J. Fluid Mech. (2010), *vol.* 645, *pp.* 479–496.
doi:10.1017/S0022112009992862

Laboratory experiments and a non-harmonic theory for topographic Rossby waves over a linearly sloping bottom on the *f*-plane

YAIR COHEN[1], NATHAN PALDOR[1]†
AND JOËL SOMMERIA[2]

[1]The Fredy and Nadine Herrmann Institute of Earth Sciences, Edmond J. Safra Campus, Givat Ram,
The Hebrew University Jerusalem, Jerusalem 91904, Israel

[2]Laboratoire des Ecoulements Géophysiques et Industriels (LEGI, CNRS-INPG-UJF) BP53 38041,
Grenoble CEDEX 9, France

(Received 22 February 2009; revised 19 October 2009; accepted 19 October 2009;

Low-frequency waves that develop in a shallow layer of fluid, contained in a channel with linearly slopping bottom and rotating with uniform angular speed are investigated theoretically and experimentally. Exact numerical solutions of the eigenvalue problem, obtained from the linearized shallow water equations on the *f*-plane, show that the waves are trapped near the channel's shallow wall and propagate along it with the shallow side on their right in the Northern hemisphere. The phase speed of the waves is slower compared with that of the harmonic theory in which bottom slope is treated inconsistently. A first-order approximation of the cross-channel dependence of the coefficient in the eigenvalue equation yields an approximation of the cross-channel velocity eigenfunction as an Airy function, which, for sufficiently wide channels, yields an explicit expression for the wave's dispersion relation. The analytic solutions of the eigenvalue problem agree with the numerical solutions in both the wave trapping and the reduced phase speed. For narrow channels, our theory yields an estimate of the channel width below which the harmonic theory provides a more accurate approximation. Laboratory experiments were conducted on a 13 m diameter turntable at LEGI-Coriolis (France) into which a linearly sloping bottom of 10 % incline was installed. A wavemaker generated waves of known frequency at one end of the turntable and the wavenumbers of these waves were measured at the opposite end using a particle imaging velocimetry technique. The experimental results regarding the phase speed and the radial structure of the amplitude are in very good agreement with our theoretical non-harmonic predictions, which support the present modification of the harmonic theory in wide channels.

1. Introduction

The existence of low-frequency waves in a layer of fluid over a sloping bottom has been established in the framework of a harmonic theory where the depth variations induce vorticity gradients similar to that of the β-term in planetary waves (Rhines 1970; Gill 1982; Pedlosky 1986). The low-frequency waves that develop in a layer of fluid where the depth (thickness) is non-constant are therefore called topographic

---

† Email address for correspondence: nathan.paldor@huji.ac.il

Rossby waves (TRW). Their name highlights the fact that these waves originate from changes in (potential) vorticity caused by the variations in the height (thickness) of a water column, as it moves up and down the shelf. The low-frequency TRW belong to a wider class of coastally trapped waves whose high frequency members include Kelvin waves, edge waves and inertia–gravity waves. Observations of TRW were reported on continental shelves throughout the world. The early observations followed the analysis of records from two tide-gauges located along a coast. Examples of such observations include the east Australia coastline (Hamon 1962), the west Australia coastline (Hamon 1966), the coast of North Carolina (Mysak & Hamon 1969) and the coast of Oregon (Mooers & Smith 1968). The existence of TRW was also demonstrated in current meter observations reported by Cartwright (1969) in St. Kilda (Scotland) and by Cutchin & Smith (1973) along the coast of Oregon. The observed TRW propagate parallel to the shoreline with the coast on the right (respectively left) in the northern (respectively southern) hemisphere.

In this study, we develop a non-harmonic theory for TRW in a channel on the f-plane, i.e. when the rotation vector is spatially uniform and two walls bound the layer of fluid. This set-up is fairly easy to construct in laboratory experiments carried out on a cylindrical turntable with sloping bottom. From a theoretical viewpoint, this set-up is advantageous in that it eliminates the singularity associated with the vanishing of the mean fluid thickness at the shoreline. In the harmonic wave theory, analytical solutions for waves in a channel are found by setting all coefficients of the associated eigenvalue equation to constants (see Pedlosky 1986; Cushman-Roisin 1994). In order to account for the case of a slightly sloping bottom, the mean height of the fluid is assumed constant everywhere, while the derivative of the mean height is taken to be non-zero (but constant) to enable the potential vorticity to change (and TRW to form). The assumption of a nearly constant mean depth (height) limits the applicability of this theory to narrow channels with gently sloping bottoms only. In addition to the apparent inconsistency of the harmonic theory, where the depth is assumed constant everywhere in the equations but its derivative is assumed non-zero, this assumption has also been shown to violate energy conservation (Staniforth, Williams & Neta 1993). Exact analytical solutions of harmonic waves were obtained for non-divergent flows by Buchwald & Adams (1968) for a channel with an exponentially sloping bottom. Both this theory and the divergent harmonic ones yield similar dispersion relations in which the frequency vanishes for very small, as well as for very large wavenumbers, and the maximal frequency occurs at some finite wavenumber for all modes.

Numerical solutions for divergent flows in a channel with an exponentially sloping bottom were calculated by Caldwell, Cutchin & Longuet-Higgins (1972). The resulting dispersion curves are similar to those of the non-divergent theory, but the frequencies are lower by up to 20 % compared with those of the analytic non-divergent theory (the difference varies with the model parameters).

The harmonic analysis of TRW over linearly sloping bottoms (Pedlosky 1986) was extended numerically to the non-harmonic regime by Staniforth *et al.* (1993), who solved the eigenvalue equation numerically. These solutions clearly demonstrate that the harmonic approximation is valid only for gently sloping bottoms, and that the non-harmonic functions are the confluent hyper-geometric functions instead of harmonic (sine and cosine) ones. However, this finding does not simplify the eigenvalue problem sufficiently so as to yield an explicit expression for the dispersion relation of the non-harmonic waves. A non-harmonic theory for the planetary Rossby waves on the β-plane was developed by Paldor, Rubin & Mariano (2007) by solving the eigenvalue, Schrödinger, equation numerically. Explicit expressions for the dispersion relations of the non-harmonic planetary waves were derived by linearly expanding the potential of the relevant Schrödinger equation about the equatorward boundary (Paldor & Sigalov 2008). This expansion allows the formulation of an explicit expression for the dispersion relation of the non-harmonic waves, whose amplitudes are trapped near the equatorward boundary so that the dispersion relation becomes independent of the channel width for sufficiently wide channels. An application of this approach to spherical coordinates has yielded explicit expressions of the dispersion relations that have no harmonic counterpart (De-Leon & Paldor 2009). As pointed out above, in terms of vorticity generation, the variation of $f(y)$ in the planetary wave problem is analogous to the variation of $H(y)$ in TRW (where H is the mean thickness of the fluid and y is the cross-channel coordinate). Thus, it is natural to apply the same method used for deriving the characteristics of planetary waves on the β-plane or the sphere to topographic waves with a non-constant H. The non-harmonic theory developed in the present study complements the study of Staniforth *et al.* (1993) by deriving explicit expressions for the dispersion relations and validating these expressions by comparing them to laboratory results. Since the slope of the linear bottom profile in our theory is arbitrary, the theory provides a first-order approximation to any realistic bottom slope.

The generation of TRW in laboratory experiments is done by forcing a displacement of the fluid from its mean thickness. Such experiments were previously carried out in a flat-bottom annulus in which depth variations were generated by rotating the fluid, which produced the necessary radial thickness variations (see Ibbetson 1967; Platzman 1968). The results of Ibbetson's experiments were in good agreement with the divergent rotating theory of Phillips (1965). The results of a more advanced experimental set-up in which the bottom slope is exponential were reported by Caldwell *et al.* (1972). These results showed good agreement between the experimental results and numerical solutions of the eigenvalue problem.

This paper is organized as follows. Following the formulation of the eigenvalue problem in § 2 for any linear $H(y)$, we proceed in § 3 to the application to TRW of the method used in the study of non-harmonic planetary waves, which yields an explicit expression for the dispersion relation of the non-harmonic TRW. In § 4 we describe a set of experiments carried out in a turntable with a linearly sloping bottom that correspond to the theory developed in § 3. We end in § 5 with a discussion of the theoretical and experimental results.

2. Formulation of the model and the eigenvalue equation

The physical set-up of the problem is shown in figure 1, where x^* and y^* are the long channel and cross-channel horizontal Cartesian coordinates, respectively (x^* is positive when the shallow wall is on its right), u^* and v^* are the corresponding velocity components in these directions. η^* is the displacement of the free surface from its mean height $H^*(y) = H_0 + H'y^*$ where H' (a positive constant) is the derivative of $H^*(y)$ with respect to y^* and H_0 is the water depth at $y^* = 0$ (the shallow wall).

The linear shallow water equations (LSWE) that describe the dynamics of a thin layer of fluid (i.e. Euler equations with rotation for a shallow layer of incompressible fluid) are

$$\frac{\partial u^*}{\partial t^*} - f v^* + g\frac{\partial \eta^*}{\partial x^*} = 0, \tag{1a}$$

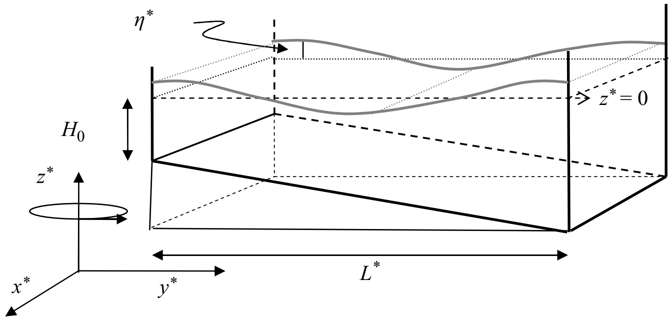

FIGURE 1. A cross-section of the channel, including the definition of the (dimensional) model parameters. The right-hand Cartesian coordinate system and rotation are shown on the left. The cross-channel velocity vanishes at the two channel boundaries and the channel width is L^*. The mean depth, which varies linearly in the cross-channel direction, is uniform in the (infinite) long-channel direction.

$$\frac{\partial v^*}{\partial t^*} + f u^* + g \frac{\partial \eta^*}{\partial y^*} = 0, \tag{1b}$$

$$\frac{\partial \eta^*}{\partial t^*} + H^* \left(\frac{\partial u^*}{\partial x^*} + \frac{\partial v^*}{\partial y^*} \right) + H'v = 0, \tag{1c}$$

where f is the (constant) Coriolis frequency and g is the gravitational constant (the reduced gravity in equivalent barotropic cases). To minimize the number of parameters in system (1), we non-dimensionalize it by scaling variables as follows: The depth scale is taken as H_0 (the depth at $y = 0$), time scale is f^{-1}, the velocity components scale is $\sqrt{gH_0}$ and the horizontal length scale is the radius of deformation, $R_d = \sqrt{gH_0}/f$. The following non-dimensional system that results from this scaling of system (1) (the non-dimensional variables are denoted similar to the dimensional ones but without the asterisk) has a single non-dimensional parameter α:

$$\frac{\partial u}{\partial t} - v + \frac{\partial \eta}{\partial x} = 0, \tag{2a}$$

$$\frac{\partial v}{\partial t} + u + \frac{\partial \eta}{\partial y} = 0, \tag{2b}$$

$$\frac{\partial \eta}{\partial t} + (1 + \alpha y) \left(\frac{\partial u}{\partial x} + \frac{\partial v}{\partial y} \right) + \alpha v = 0. \tag{2c}$$

Here, $1 + \alpha y$ is the non-dimensional mean depth and the non-dimensional parameter $\alpha = H' R_d H_0^{-1}$ incorporates the bottom slope, the horizontal length scale and the depth scale. Our velocity scale, $\sqrt{gH_0}$, is the phase speed of Kelvin waves (or gravity waves) at $y = 0$. Since all the coefficients are independent of x, the long channel direction, it is natural to assume harmonic solutions in the long channel direction for all three variables, i.e. u, v, $\eta \sim \exp^{\mathrm{i}(kx - \omega t)}$, where k is the wavenumber, c is the phase speed (so $\omega = ck$ is the frequency). This form of solution enables us to represent the temporal and x derivatives as multiplication by the frequency and wavenumber, respectively. Letting $(\partial/\partial x) = \mathrm{i}k$, $(\partial/\partial t) = -\mathrm{i}\omega$ and defining $V = \mathrm{i}v/k$ in system (2) yields the (real) system:

$$c u - V - \eta = 0, \tag{3a}$$

$$u - k^2 c V + \frac{\partial \eta}{\partial y} = 0, \tag{3b}$$

$$-(1+\alpha y)u+(1+\alpha y)\frac{\partial V}{\partial y}+\alpha V+c\eta=0. \tag{3c}$$

Equation (3*a*) yields $u=(V+\eta)/c$, which can be used to eliminate u in (3*b*) and (3*c*). The result is the following pair of first-order differential equations:

$$\frac{\partial\eta}{\partial y}=-\eta\frac{1}{c}+V\left[k^2c-\frac{1}{c}\right], \tag{4a}$$

$$\frac{\partial V}{\partial y}=\eta\left[\frac{1}{c}-\frac{c}{1+\alpha y}\right]+V\left[\frac{1}{c}-\frac{\alpha}{1+\alpha y}\right]. \tag{4b}$$

The value(s) of c in system (4) can only be determined by imposing two boundary conditions (hereafter BC) on the general solutions of this differential set, which for the case of a channel are simply the vanishing of V at the two channel walls. We find it convenient to derive a single second-order equation for V (rather than for η, as was done by Staniforth *et al.* 1993) since it simplifies the form of the two BC at the channel walls. The resulting second-order equation enables one to examine analytically the characters of the system's solutions by viewing it as a Schrödinger equation whose potential is expanded to first-order in y. This expansion provides an approximation for the eigenfunctions in wide channels (similar to the way Paldor & Sigalov 2008 found approximate solutions for planetary waves) and yields a simple approximate expression for the dispersion relation of these waves that can be compared with observations. Towards this end, system (4) is rewritten for the cross-channel volume transport $\tilde{V}=V(1+\alpha y)$ and reduced to a single second-order equation for $\tilde{V}$ by differentiating equation (4*b*) and eliminating both η and $\partial\eta/\partial y$. Neglecting quadratic terms in $\omega=ck$ (which limits our solutions to low-frequency waves only) we get

$$\frac{\partial^2\tilde{V}}{\partial y^2}=\frac{\partial\tilde{V}}{\partial y}\left(\frac{\alpha}{1+\alpha y}\right)+\tilde{V}\left(k^2+\frac{1}{(1+\alpha y)}-\frac{\alpha}{c}\frac{1}{1+\alpha y}+\frac{1}{4}\left(\frac{\alpha}{1+\alpha y}\right)^2\right). \tag{5}$$

Letting $\tilde{V}(y)=V(1+\alpha y)=\Psi e^{ay}$ where $a=\alpha(2+2\alpha y)^{-1}$ eliminates the first derivative in the second-order equation for Ψ. If, in addition, all y-dependent terms in the Ψ-equation (i.e. the terms that multiply Ψ) are expanded to first-order in y (i.e. neglecting terms of order y^2), the resulting second-order equation for Ψ becomes

$$\frac{\partial^2\Psi}{\partial y^2}-\Psi(E+(k^2-E-\alpha^2/4)\alpha y)=0, \tag{6}$$

where the eigenvalue E is given by

$$E=1+k^2+\alpha^2/4-\alpha/c. \tag{7}$$

Since e^{ay} never vanishes Ψ has to satisfy the same BC as $\tilde{V}$. Formally, the elimination of the quadratic terms in y entails a restriction on the values of α (for the Taylor series to converge). However, the numerical results (see e.g. figure 2) show that the eigenfunctions decay fairly fast with distance from the shallow wall (i.e. they occupy a small sub-range of the channel near $y=0$ only) so the elimination of the y^2 terms is of wider applicability than can be formally justified based on the maximum values of y (i.e. L) and α.

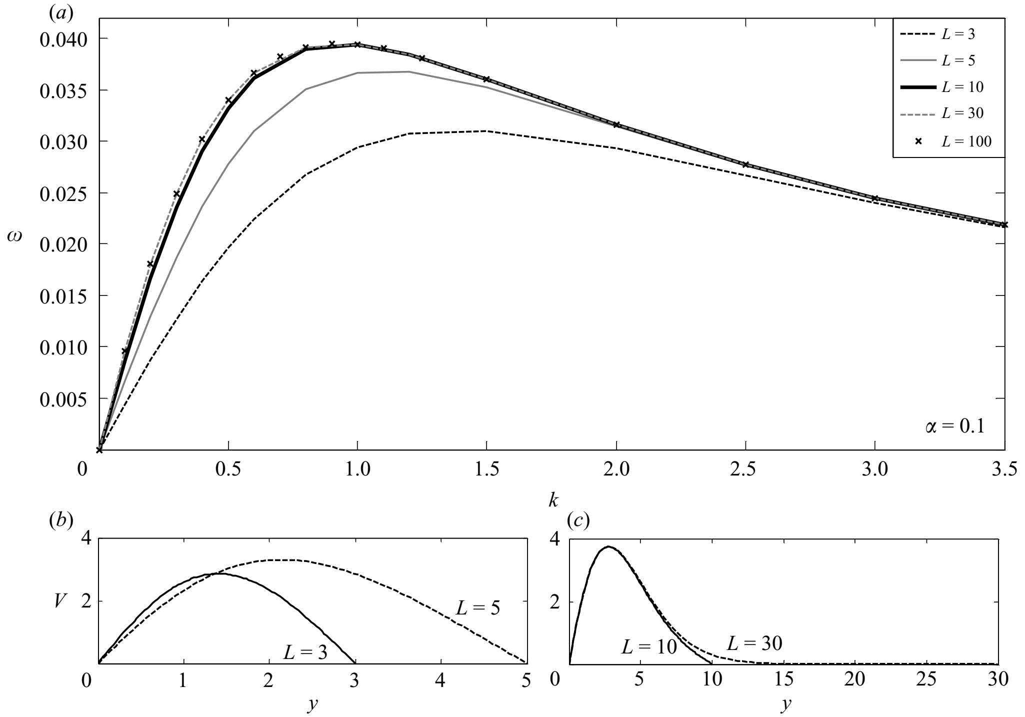

FIGURE 2. (*a*) Numerically calculated dispersion relations of the first ($n = 0$) TRW mode for different channel widths (L) with $\alpha = 0.1$. (*b,c*) Numerically calculated amplitudes (eigenfunctions) of the cross-channel velocity, $V(y)$, at $k = 1$ for $L = 3$, $L = 5$ (*b*, where the abscissa extends only to $y = 5$) and $L = 10$, $L = 30$ (*c*, where the abscissa extends to $y = 30$). The arbitrary normalization used in all cases is $\eta(y = 0) = 0.1$.

3. Numerical and analytical solutions

The (η, V) system, (4), is a set of ordinary differential equations (ODE) in y that can be easily integrated numerically from one channel wall starting with $V = 0$ (and say, $\eta = 0.1$ as an arbitrary normalization) to the other wall, and the value of c is then varied so as to satisfy $V = 0$ BC there. Here, the integration is performed by using MATLAB's function BVP4C which integrates the equations and finds the value of c for which V vanishes at the deep wall. The BVP4C, function solves the ODE system and the associated boundary condition as a boundary value problem using a fourth-order collocation method. The accuracy of this solution was confirmed by directly integrating the ODE using a fifth-order Runge–Kutta integrator into which the value of c from the BVP4C solution is inserted and verifying that V vanishes at the deep wall as required.

Numerical solutions of the eigenvalue problem present both the values of the phase speed that yield the dispersion curves $c(k)$ and the eigenfunctions $u(y)$, $V(y)$ and $\eta(y)$. Three well-known wave types are found in the results: the non-dispersive Kelvin waves, the dispersive, high-frequency Poincare waves and the dispersive, low-frequency TRW. The identification of the wave type (i.e. Poincare, Kelvin or TRW) is done according to the value of the frequency. Since the time scale is the Coriolis frequency, wave solutions with frequencies higher than unity are identified as Poincare waves and wave solutions with frequencies lower than unity are identified as TRW. Kelvin waves are clearly identified by the cross-channel velocity eigenfunction since V vanishes almost everywhere across the channel. The index of the mode (n) is determined by the number of zero crossings of $V(y)$. Since this study focuses on TRW, the solutions for the high frequency wave types (Kelvin and Poincare) found in our numerical solutions are not shown.

In figure 2(a) the dispersion relations, $\omega(k)$, of the first ($n=0$) mode are shown for the indicated values of channel widths, L, and for $\alpha=0.1$. These results show that for given, sufficiently small, k the frequency first increases with the channel width, but at $L>10$, the frequency practically converges to an asymptotic value. Both the small difference between the curves of $L=10$ and $L=30$ and the complete overlap between the x marks (that represent the dispersion relation for $L=100$) and the $L=30$ curve clearly substantiate these findings. In figure 2(b,c) the corresponding structure of the $V(y)$ eigenfunctions for $k=1$ is compared: for narrow channels ($L=3$ vs. $L=5$) in figure 2(b) and for wide channels ($L=10$ vs. $L=30$) in figure 2(c). For $L<10$, the eigenfunction's structure is very close to harmonic with the maximal amplitude near the centre of the channel (figure 2b). As L increases ($L\geqslant 10$), the structure of eigenfunctions becomes trapped near the shallow wall with the location of maximal amplitude limited to $y\approx 3$ (figure 2c). These qualitative features of the eigensolutions typify other values of α and they persist for other modes (results not shown). The results clearly indicate the existence of non-harmonic solutions to the eigenvalue equation for some values of the parameters α and L.

A harmonic approximation to (6) is easily constructed by neglecting the αy term in the coefficient of Ψ (so the equation has constant-coefficients). When this is done, the eigensolutions are given by trigonometric functions and the imposition of the BC at the two walls yields the dispersion relation for the frequency as a function of α, k and L, which for mode n (that has n zero crossings of V in the channel) becomes

$$\omega=\frac{\alpha k}{1+k^2+(n+1)^2\pi^2/L^2}. \tag{8}$$

Equation (8) is found in various textbooks (e.g. Pedlosky 1982; Cushman-Roisin 1994) as the classical harmonic solution for the dispersion relation of TRW. Here, n (mode number) represents the number of nodal points (zero crossing) of the $V(y)$ eigenfunction, and it is clear that the phase speed decreases with the mode number. The sign of the phase speed equals the sign of α; hence, in the northern hemisphere ($f>0$), the waves propagate along the channel with the shallow wall on the right (and on the left in the southern hemisphere).

It should be emphasized that this harmonic solution is obtained by neglecting αy in (6), which is valid only in narrow channels with gentle slopes (but no estimate exists of how small α should be for this approximation to hold). The eigenfunctions shown in figure 2 demonstrate that as the channel width, L, increases the harmonic solution does not provide an accurate approximation to the exact one. The effect that the increase in L has on the dispersion curves is shown in figure 3, from which it is clear that in the non-harmonic regime (large α or L) the phase speed is much smaller than the harmonic ones (for the same value of k). In order to approximate analytically the non-harmonic solutions, the αy term in (6) must be retained. Since in this case the coefficient of Ψ is linear with respect to y, a transformation of this equation to an Airy equation (similar to that employed by Paldor & Sigalov 2008 and De-Leon & Paldor 2009 in their study of planetary waves) should also be possible. We thus transform (6) to

$$\frac{\partial^2\Psi}{\partial Z^2}-Z\Psi=0, \tag{9}$$

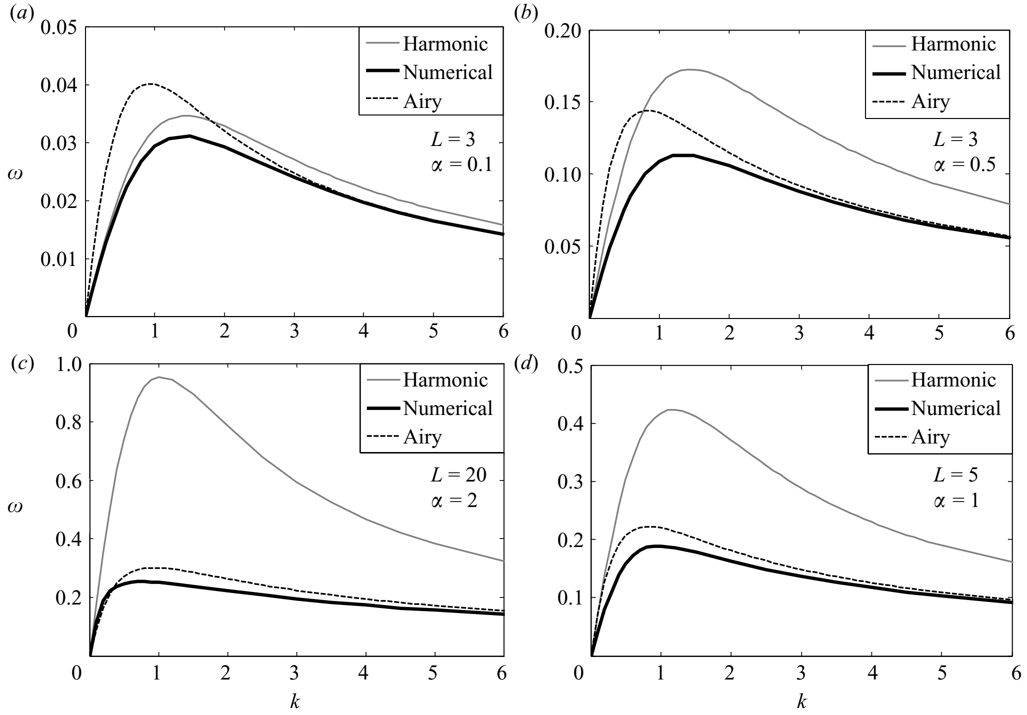

FIGURE 3. The dispersion relations of the $n = 0$ TRW mode for the indicated values of α and L: the exact numerical solution (solid black line) harmonic approximation ((8); solid grey line) and non-harmonic, Airy-function, approximation ((11); dashed line). The harmonic solution yields reasonably accurate approximation only at small α and L (and not too large k).

where Z is defined by

$$Z(y) = (k^2 - E - \alpha^2/4)^{-2/3})\alpha^{-2/3}(E + (k^2 - E - \alpha^2/4)\alpha y). \tag{10}$$

The solutions of (9) are Airy functions $Ai(Z)$ and $Bi(Z)$ shown in figure 4(*a*). Both functions oscillate for negative Z, while for positive Z, Ai decays monotonically and Bi grows monotonically (both at a rate faster than exponential; see e.g. Abramowitz & Stegun 1972). These realizations are now used to construct the non-harmonic solution similar to the way it was done by Paldor & Sigalov (2008) and De-Leon & Paldor (2009) in the study of non-harmonic planetary waves, and the interested reader is referred to these works for more details on the approach. Briefly, the general solution of (9) is a linear combination of $Ai(Z)$ and $Bi(Z)$ (i.e. $A_0Ai(Z) + B_0Bi(Z)$, for some constants A_0 and B_0) and this general solution has to vanish at both boundaries. When the deep wall is located at large positive $Z(y = L)$, where $Ai(Z(L)) \ll 1 \ll Bi(Z(L))$ (see figure 4*a*) B_0 must be negligibly small, of order $Ai(Z(L))A_0/Bi(Z(L))$, i.e. $B_0Bi(Z)$ can be neglected in the linear combination. In this case, the solution of (9) is well approximated by $Ai(Z)$ only and the deep wall BC is trivially satisfied by Ai alone. The BC at the shallow wall is satisfied only if $y = 0$ transforms into one of the zeros of $Ai(Z)$. The zeros of Ai (marked as Z_n) are listed in the literature and the first three, shown in figure 4*a*, are $Z_0 = -2.3811$, $Z_1 = -4.08795$, $Z_2 = -5.5205$ and $Z_3 = -6.67867$.

To justify the neglect $Bi(Z)$, we require that the deep wall be located at $Z \geqslant 4$ where the vanishing of the solution implies that the contribution of $Bi(Z)$ in the linear

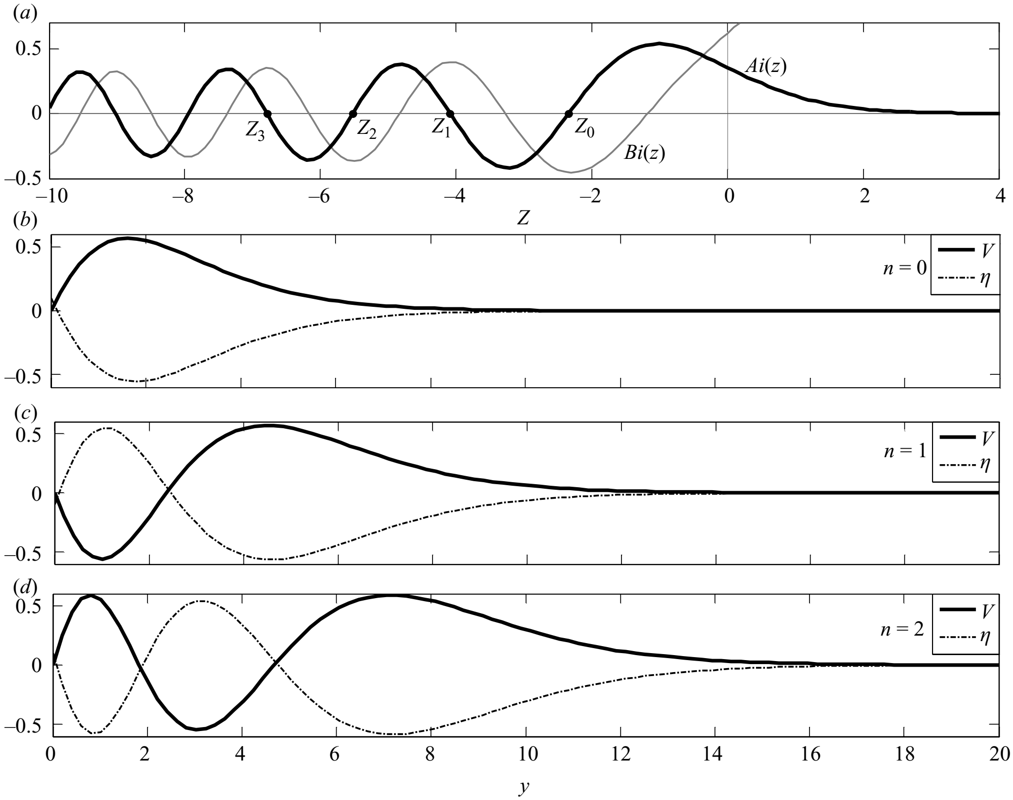

FIGURE 4. (*a*) The Airy functions $Ai(Z)$ (black curve) and $Bi(Z)$ (grey curve). For negative Z values, both functions are oscillatory while for positive Z values $Ai(Z)$ is decaying and $Bi(Z)$ is growing. (*b–d*) Numerically calculated eigenfunctions of the first three TRW modes in a channel. The vertical displacement (η) eigenfunctions are given by the dash-dotted curves and that of the cross-channel velocity (V) by the solid curves. The parameter values are $L=20$, $k=1$ and $\alpha=0.5$ and the normalization values (η at $y=0$) are chosen as 0.1 in the first and third modes and -0.1 in the second mode to demonstrate the similarity between the V profiles and $Ai(Z)$ in (*a*).

combination is $O(10^{-8})$ compared with $Ai(Z)$. This choice of deep wall location also guarantees that the BC is satisfied since $Ai(4)\approx 10^{-4}$.

In order for the Airy function approximation to be valid, the term $k^2-E-\alpha^2/4$, which multiplies αy in the coefficient of Ψ in (6), has to be positive. If we further assume that $E+\alpha^2/4$ is negligible compared with k^2 in the $Z(y)$ transformation (see (10); we will verify this below), then a simple formula for the dispersion relation for TRW is obtained:

$$\omega=\frac{\alpha k}{1+k^2+\alpha^2/4+k^{4/3}\alpha^{2/3}|Z_n|}. \tag{11}$$

Equation (11) yields an explicit expression for the phase speed $c=\omega/k$. To validate it, we substitute this expression into (7) and examine the conditions under which $E+\alpha^2/4$ is indeed negligible compared to k^2. The resulting condition is: $k^2\gg\alpha^2/(4|Z_n|k^{-2/3}\alpha^{2/3}+4)$, which is satisfied for $k>0.01$, 0.1, 0.18, 0.35 when $\alpha=0.1$, 0.5, 1 and 2, respectively. These values of α are used in figure 3, where we compare the exact, numerically computed, dispersion relation (solid curves) with

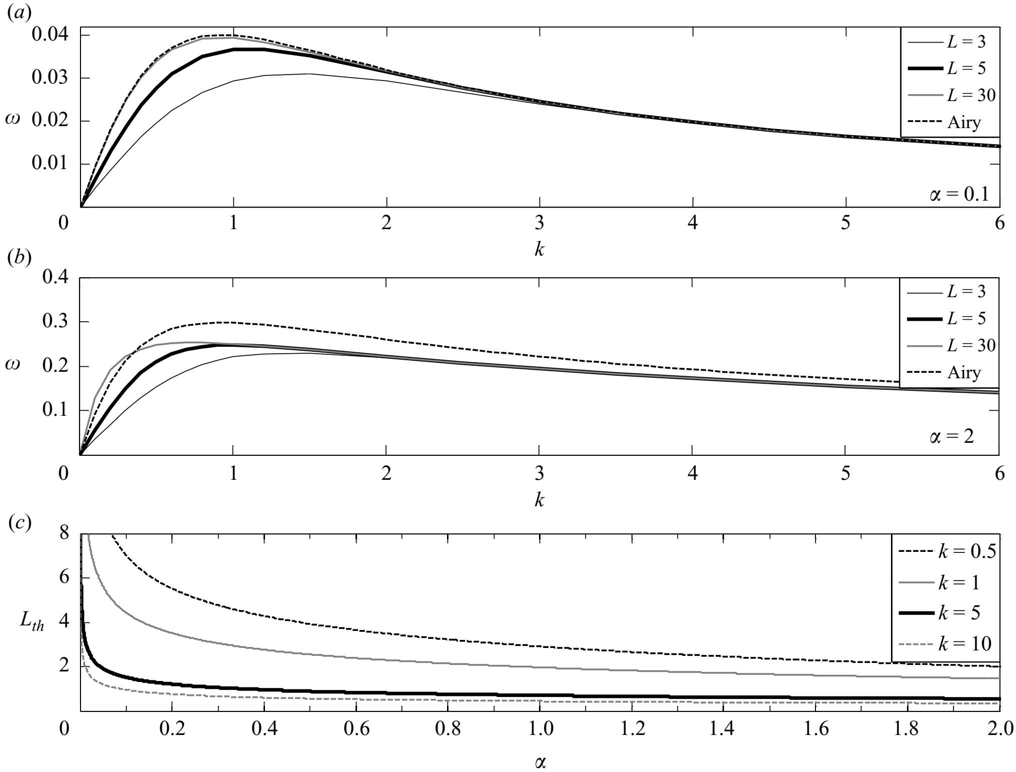

FIGURE 5. (a,b) Numerically calculated dispersion relations of the first TRW mode for the indicated channel widths (L) (solid lines). Also shown are the non-harmonic (Airy) approximations ((11); dashed lines) for the indicated α-values (these approximations are independent of L). (c) The values of $L_{th}(\alpha)$ as given by (12) for the indicated k-values.

the harmonic relation (8), (grey curves) and the Airy dispersion (11), (dashed curves). The comparison clearly demonstrates that the non-harmonic dispersion relation, (11), provides a much more accurate estimate to the exact solution than the harmonic relation, (8), for sufficiently wide channels and for sufficiently large α. Note that in figure 3(c) where $\alpha = 2$, the above formal condition for the validity of the non-harmonic solution is not satisfied for $k < 0.35$, yet it provides a more accurate estimate than the harmonic solution at all k values.

In figure 5, we compare the non-harmonic dispersion relations with the exact numerical solutions for different channel widths (figure 5a,b). It is clear from (11) that the non-harmonic relation is independent of the channel width, L and for small $\alpha(=0.1$; figure 5a) the numerical solutions approach the Airy estimate as L increases (even for $L = 5$, the curves are quite similar at $k > 1.5$). In contrast, for large value of $\alpha(=2$, figure 5b) the error in the estimate is noticeable even for very wide channels (e.g. $L = 30$) and for both large and small k. Yet, the non-harmonic solution is a much better approximation to the exact (numerical) one compared with the harmonic solution for the same parameter values (see figure 3c for a three-way comparison at the same α).

Since the non-harmonic dispersion relation in (11) is independent of L while the harmonic relation in (8) increases with $L,$ it is possible to find a threshold channel width (L_{th}) at which the two solutions are identical for a given wavenumber, k.

Since for $L > L_{th}$ the harmonic frequency is larger than the non-harmonic one (for a given value of k), this threshold value is the minimal channel width for which the non-harmonic solution provides a more accurate approximation than the harmonic solution. This threshold channel width, L_{th} (which varies with the values of α, k and the mode number, n), is given by

$$L_{th}(\alpha, k) = (n+1)\pi \left(\alpha^2/4 + |Z_n| k^{4/3} \alpha^{2/3}\right)^{-1/2}. \tag{12}$$

The dependence of this threshold channel width on α for different wavenumber values is presented in figure 5(c).

The Airy-function approximation for the amplitude of the eigenfunction, $V(y), (= Ai(Z(y)))$ decays for positive Z faster than exponential for all n. Hence, the above analysis implies that for all TRW modes, the wave amplitude vanishes sufficiently far from the shallow wall even though the sloping bottom (which generates the mean vorticity as explained in the Introduction) exits there. These theoretical characteristics are quite obvious in the numerical solution for the eigenfunctions as shown in figure 4(b–d). Also evident from a comparison of figure 4(a–d) is that the variations of mode n (where $n = 0$, 1 or 2) are very well approximated by $Ai(Z)$ provided the shallow wall is placed right at Z_n and regardless of the location of the deep wall.

4. Laboratory experiments

In the laboratory experiments described here, the waves are generated mechanically in one end of a cylindrical turntable with sloping bottom while the wavenumber is observed at another end of the turntable. By varying the generating frequency we get a $k(\omega)$ relation that is the inverse of the theoretical $\omega(k)$ dispersion relation (this generation-observation approach was also used by Phillips 1965 and Caldwell *et al.* 1972). For the circle located in the centre of the slope (radius of 4 m), these waves travel some 15 m from the generating point at one end of the tank to the observation point located at the opposite the end of the tank (see figure 6). The observed inverse dispersion relations are then compared to a numerical theory that solves the governing equations (system 4) for the specific set-up shown in figure 6, in which the sloping bottom occupies the shallowest, outermost, 4 m while in the remaining 1.5 m located closer to the centre of the tank the bottom is flat.

4.1. *The experimental set-up and method of analysis*

The experiments were performed in an annulus that occupies the outer 5.5 m of a 6.5 m cylindrical tank and the maximal water depth in the annulus (and in the tank) is 1 m (see figure 6). In the outer periphery, a 4 m wide conical bottom with a 10 % slope was introduced into the tank so that the maximal water depth at the shallow (outer) wall is reduced by 0.4 m (i.e. it is 0.6 m). The tank is placed on a rotating platform whose radius is 7 m that rotates counterclockwise with a controlled (variable) angular speed, with minimal periods of about 30 s. The system is equipped with an anti-precession mechanism that maintains speed uniformity to better than 10^{-4} of the rotational frequency. Heavy plastic curtains were hung above the outer wall of the turntable to isolate the air above the tank from the air outside of it so as to minimize friction between the water in the tank and the overlying air. For the rotation speeds used in the experiments, the curvature of the water surface is of order 2–5 cm, which adds a tiny (negligible) variation to the water thickness compared with the variations that result from the bottom slope.

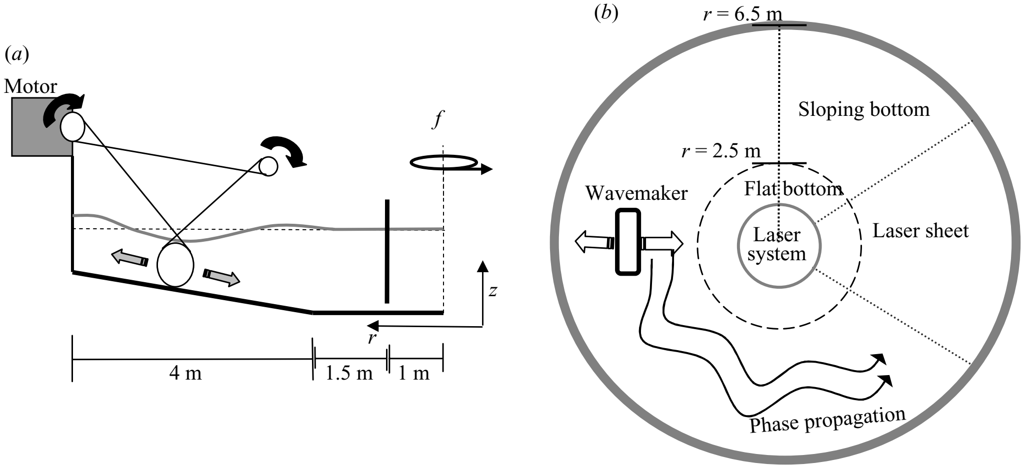

FIGURE 6. Radial cross-section (*a*) and a planar top view (*b*) of the tank. The location of the separation between the sloping bottom part and the flat bottom part as well as the radial location of the inner wall are given on the radial cross-section. The radial motion of the wavemaker up and down the slope generates waves that travel azimuthally towards the measurement area indicated by 'laser sheet' in the planar top view. Both sketches are not to scale.

The generation of waves uses a similar procedure to that used by Caldwell *et al.* (1972). Water is displaced in the radial direction by rolling a heavy rod up and down the sloping bottom using a 500 Hz electric motor (CEM 83V) whose output frequency is divided by 480 using two chain-saw wheel systems. The generated period and amplitude were controlled externally by LABVIEW software (see e.g. Sumathi & Surekha 2007). The up-and-down movement of water columns across isobaths creates disturbances that propagate along isobaths around the tank to the measurement area located at the opposite side of the tank (see figure 6*b*). Since there are many cases in which a single frequency has two corresponding wavenumbers (see e.g. figure 3), both the location of the rolling rod and its length (i.e. long or short) were changed so as to fit the theoretically relevant wavenumber. Towards that end, two types of rods were used to generate waves with the same frequency but different wavelength (wavenumber): A 2 m long, 20 cm diameter, rod (the long rod used for generating long waves) and a 0.4 m long 15 cm diameter rod (the short rod used for generating short waves). In all cases, the rods were centred at the location of maximal amplitude as predicted by the numerical theory. In two of the experiments in which we attempted to generate the second ($n = 1$) mode, the waves were generated by two short rods that were oppositely connected to the motor and placed parallel to each other at two isobaths, which is the way Caldwell *et al.* (1972) generated their second mode.

The horizontal velocities were measured in the observation area of the tank using a particle imaging velocimetry (PIV) technique that consists of particles (used to trace the fluid flow), an illuminating laser sheet and a camera.

The density of the polystyrene (600 μm) particles used as tracers was adjusted to be slightly denser than the water and the particles were subsequently distributed in the water shortly prior to the onset of the experiment. The minute density difference minimizes the number of particles that might stay at the water surface while being pushed around by the relative motion of the overlying air. This air-induced motion of the tracer particles might have masked the experimental results that are concerned with the water motion, observed by following the particles. After every 20 experiments, the water was changed to enable the removal of particles that had sunk to the bottom of the tank during those experiments.

The laser beam is generated with a *Millennia 6W* solid laser generator whose wavelength is 532 nm. The laser sheet is produced by a *6850, Cambridge technology* mirror galvanometer (a controlled rotating mirror) located in the centre of the tank that creates an 18° sheet of green light at the required water depth. The mirror frequencies were adjusted to the exposure time of the camera so that at least two cycles of the mirror were completed in each exposure. All experiments were performed under dark conditions.

The camera used in our experiments is a wide angel (17°) Nikon D200 camera (10 mpixel) positioned above the tank and rotating with it while covering most of the area illuminated by the laser. The rate of camera shots was controlled by Nikon software, which was programmed to take a frame every 5 s.

The identification of the period, wavenumber and amplitude of the waves generated (and observed) as described above was done by analysing the digital images using the 'UVMAT' software self-produced in LEGI-Coriolis, which processes the original images and generates velocity fields using correlation imaging velocimetry method. From the calculated velocity fields, the software generates velocity time series on a grid of points and for complete cycles of oscillation, it generates the amplitude and phase of the velocity field. Further details of the analysis and software can be found at http://www.coriolis-legi.org/CIVPROJECT/DOC_GENE/CIV_doc_lim.html, where the entire image processing method is described in full.

An important issue that should be noted here is that although the experiments are done in a cylindrical tank the software transforms the velocity vector fields into Cartesian coordinates (about a radius of 3.5 m—the centre of the slope). Accordingly, wavelengths are transformed by UVMAT from radians to metres and phase speeds from radians/second to metres/second. Thus, despite the apparent geometric mismatch, the experimental results should be compared with a Cartesian theory and not a cylindrical one.

4.2. *Experimental results*

Only two-dimensional parameters H_0 and f were varied in the various experiments described below. These two parameters, along with the constants $g(=9.81\,\mathrm{ms}^{-2})$, $L^*(=5.5\,\mathrm{m})$ and $H'(=0.1)$, determine the values of the two non-dimensional parameters: $\alpha = R_d H'/H_0$ and $L = L^*/R_d$ of the theory outlined in § 2. To help the reader to keep track of the dimensional quantities, the results of this section are presented using the non-dimensional parameters: $\omega^*/f = \omega$, $L^*/R_d = L$ and $k^* R_d = k$. The value of $\alpha = 0.1 R_d/H_0$ equals $0.313(H_0)^{1/2} f^{-1}$.

The laboratory set-up includes both a slope region and a flat bottom region, which mandates a more complicated BC at the deep side than that considered in the analytic theory. An analytical solution of this complex geometry is not available but a numerical solution is as easy to compute as in the case of a channel with uniformly sloping bottom described above. The experimental results are therefore compared with numerical solutions of the eigenvalue problem in which the non-dimensional width includes both the slope and the flat parts of the radial ranges of the annulus (i.e. $L = 5.5\,\mathrm{m}/R_d$). The analytical dispersion relations given above were computed for the harmonic theory with $L = 4\,\mathrm{m}$ (i.e. only the sloping segment) and non-harmonic (Airy) theory (where the width is not a model parameter). It should be pointed out that a comparison of the experiments conducted with the complex BC at the deep side

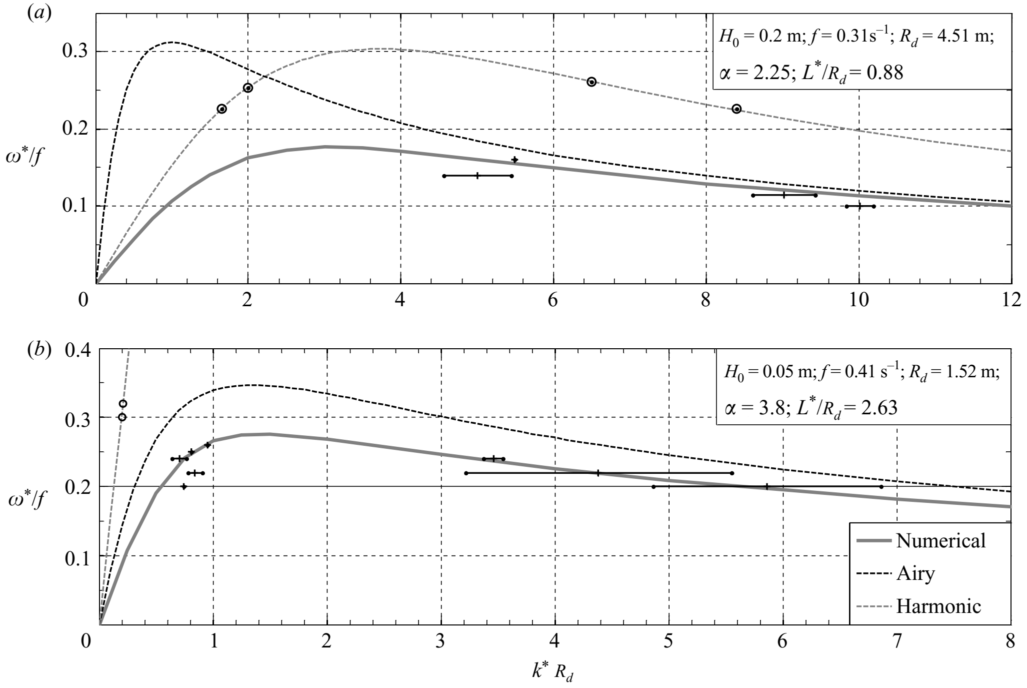

FIGURE 7. A comparison between the harmonic ((8); grey-dashed curve) and Airy-function ((11); black-dashed curve) analytic approximations, the numerical solutions (solid) and experimental results (solid error bars) for the dispersion relation of TRW in the two experimental set-ups. (*a*) Narrow channel with $L^*/R_d = 0.88$ and $\alpha = 2.25$. (*b*) Wide channel with $L^*/R_d = 2.63$ and $\alpha = 3.8$. In each set-up (i.e. panel) two experiments were carried out with forcing frequencies higher than the maximal frequency found by the numerical theory and in all these experiments no waves were observed at all. Black circles on the dashed-grey curve represent the corresponding wavenumber values predicted by the harmonic theory at these frequencies.

with the theoretical results calculated with the simpler BC cannot be easily justified. However, the expressions of these theories are the only analytical results available for comparison with the experiments, so it should not come as a surprise that the harmonic theory does not show good accuracy even for parameter values where it should be valid in the case of a simple BC (i.e. the lower wavenumber values in figure 7*a*). Perhaps, the successful match between the experimental results and the predictions of non-harmonic theory in the range of parameters satisfying the latter's validity conditions is the real surprise of this comparison (which is a result of its independence of L so the exact location of the deep wall in the flat part of the tank has no effect on the eigenfunctions).

The comparison between the experimental results and the theoretical predictions is shown in figure 7(*a,b*) for a narrow channel ($L^*/R_d = 0.88$, $\alpha = 2.25$; figure 7*a*) and a wide channel ($L^*/R_d = 2.63$, $\alpha = 3.8$; figure 7*b*). The non-dimensional wavenumbers ($k^* R_d$) are presented as horizontal error bars determined by the mean and variance of the values measured for each forcing frequency (ω^*/f). The small error in the frequency is given by the (tiny) vertical error bar. Some experiments were performed with forcing frequency higher than the maximal frequency predicted by the numerical theory, and in these cases no low-frequency waves could be detected whatsoever.

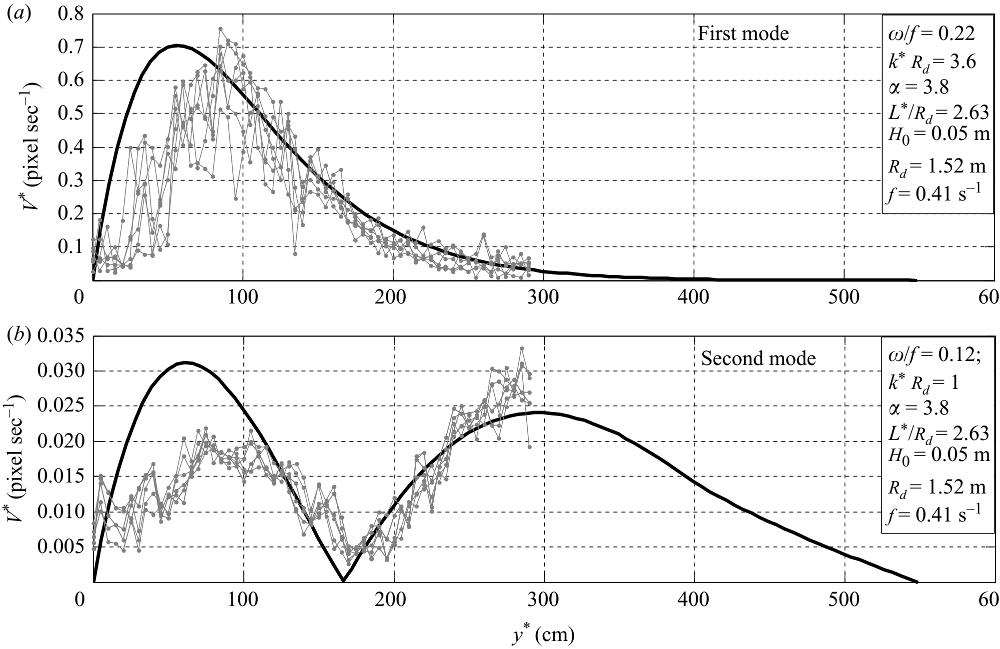

FIGURE 8. Numerically calculated absolute values of the cross-channel velocity amplitudes (solid line) compared with the observed absolute values of the cross-channel velocity amplitude (grey dotted line; 1 pixel $=2.3$ mm). The results in (*a*) are for the first mode while those in (*b*) are for the second mode. Both the numerical results and the experimental data are plotted as functions of y^* so the shallow wall is at $y^*=0$. Trapping of the waves near the shallow wall is clearly noticed in both cases. The relation between the phase speed and the maximal velocity amplitude in (*a*) is $V_{max}/c \approx 0.03$ and in (*b*) is $V_{max}/c \approx 10^{-3}$; hence, the linear approximation implicit in the LSWE (water velocity much smaller compared with the phase speed) is valid.

These experiments are shown by circles on the harmonic dispersion curve at the corresponding forcing frequencies in figure 7). For both channel widths, the agreement between the numerically calculated dispersion relations and the experimental results for $k(\omega)$ is good. Good agreement is also found between the non-harmonic analytical theory and the experiments at large wavenumbers only, since the values of α used in the experiments are high (a result of physical limitation on the dimensional parameters H_0 and f in the laboratory). The fact that no waves were observed in the experiments at frequencies above the numerically computed maxima bolsters the accuracy of the numerical predictions and highlights the irrelevance of the harmonic theory, which predicts the existence of TRW at these frequencies. The non-harmonic theory agrees with the experimental findings at high wavenumbers, where (12) (viewed as a condition for its validity in terms of the threshold value of k for a given value of L and α on its right-hand side) is satisfied.

The cross-channel structure of the cross-channel velocity (the cross-channel direction is the radial direction of the cylindrical system) is shown in figure 8, for the first ($n=0$, figure 8*a*) and second ($n=1$, figure 8*b*) modes. These experimental results estimated from complete cycles of oscillation are presented as absolute values of amplitudes, and are therefore compared with the absolute values of the corresponding numerical predication. The linear theory determines the amplitudes only up to an arbitrary normalization factor (e.g. the value of η at $y=0$). Therefore, the theoretical curves were scaled so as to fit the maximal experimental amplitudes, so only the number of nodal/maximal points and their locations should be compared. The parameter values used in these experiments correspond to those of figure 7(*b*).

The overall cross-channel structure of the velocity amplitude in both modes clearly shows trapping of the waves near the shallow wall as predicted by the numerical calculations and the non-harmonic theory. The locations of the nodal points in the numerical results are in excellent agreement with those in the experiments. In the first mode, the maximum is shifted as a result of sharp decay of the amplitude towards the outer (i.e. deep) wall, and in the second mode the relative magnitudes of the two maxima do not match the numerical prediction. This might be caused by frictional effects near the shallow wall (mainly in the first metre or so) that are filtered out in our non-viscous theory.

5. Discussion and summary

A comparison between the theoretical and experimental results shows that the LSWE model is applicable to the experimental results for long waves, provided that the mean depth is not more than 10 % of the radius of deformation. In the experiments described in the present work, as well as those reviewed in the Introduction, the waves are generated externally (forced), yet the theories to which these experiments are compared are homogeneous (free). The excellent fit between the free (homogenous) theories and the forced experiments is probably a result of a resonance that occurs when the frequency of the wave, which develops in the tank (determined by the non-dimensional model parameters, including the wavenumber), matches the forcing frequency (for a comparison of forced problems with experiments, see Pierini *et al.* 2001).

Our exact (numerical) solutions agree with the laboratory findings in narrow and wide channels, with respect to both the dispersion relation and the cross-channel structure of the amplitude. In contrast, the dispersion curves of the classical harmonic theory differ significantly from the numerical solution for either large slopes or wide channels, and in those cases the non-harmonic analytic theory provides a more accurate approximation. In the non-harmonic solution, the channel width ceases to be a model parameter once it exceeds a certain threshold value (given in (12)). Thus, for wide channels, the number of model parameters in the problem is reduced to only two: the depth at the shallow wall and the angle of the bottom slope. The non-harmonic structure and trapping of the amplitude near the shallow wall, both of which are predicted by our analysis, are confirmed by the observed amplitudes in wide channels.

The present theory predicts the existence of a threshold channel width, (12), below which the harmonic theory is accurate and above which the non-harmonic theory becomes valid. This distinction allows an informative decision, based on a simple formula, of the parameter ranges where the harmonic and the non-harmonic analytical theories should be applied to approximate the dispersion relation of TRW. For a fixed channel width, this equation provides an estimate of the threshold wavenumber above which the harmonic theory loses its validity and the non-harmonic theory becomes relevant.

In the analysis presented above, the features of the long channel velocity (u) were ignored since the wave theory is fully determined by V and η. The $u(y)$ structure

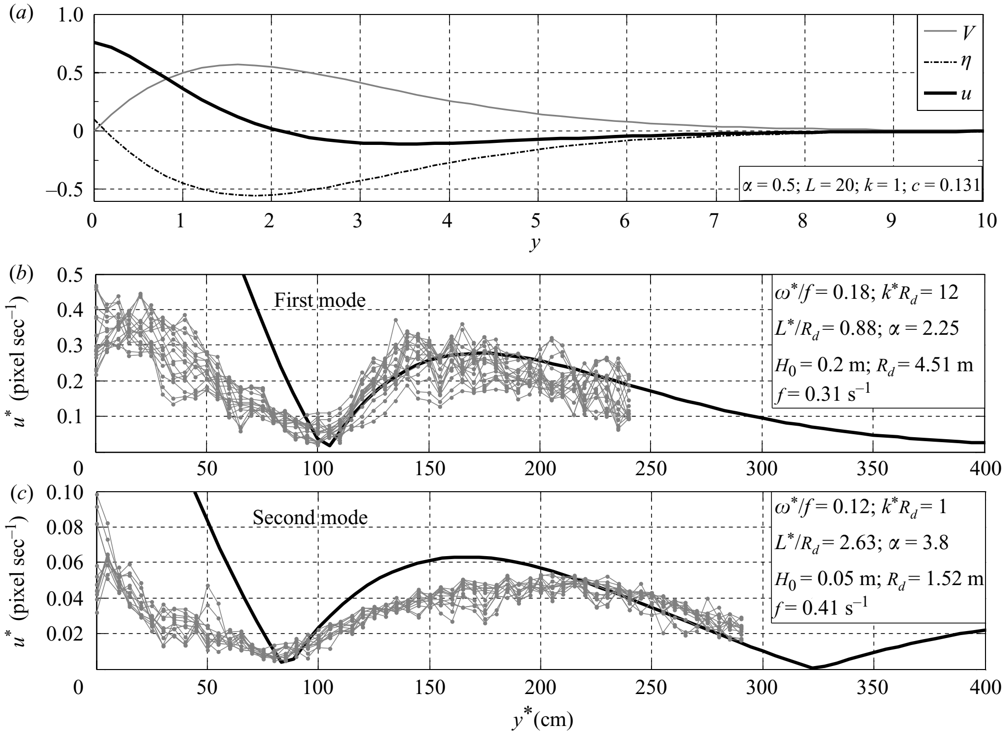

FIGURE 9. (*a*) Non-dimensional amplitudes of u, V and η as a function of y in solid black, solid grey and dash-dotted black lines, respectively. The amplitude of u (long channel velocity) is largest at the shallow wall ($y=0$) and as expected from (3*a*) $u(0)) = \eta(0)/c = 0.1/0.131 = 0.76$. (*b,c*) The numerically calculated (black solid line) cross-channel structure of the long channel velocity amplitude, $u(y)$, compared with the observed velocity (grey line with dot marks). The values of the (dimensional and non-dimensional) model parameters are indicated on the right-hand side and u is given in absolute values as before (1 pixel $= 2.3$ mm).

shown in figure 9(*a*) (black solid line) was computed from the algebraic relation in (3*a*) for the parameter values used in figure 4 with $k=1$. Two main features are obvious: First, the $u(y)$ amplitude has its maximal value at the shallow wall and at $y>0$ it oscillates with decaying maxima (and the rate of decay is faster than V and η). Second, $u(y)$ has an extra nodal point to that of V or η. Moreover, at the shallow wall where V vanishes, (3*a*) yields the simple relation $\eta/u = c$; hence, since c is smaller than unity (about 0.1), the value of u there is larger than η. These features of the $u(y)$ profile are observed in the laboratory experiments in both the $n=0$ and $n=1$ modes shown in figure 9(b, c). The comparison of the $u(y)$ profiles (in absolute values as before) between experiments and numerical results shows that in both modes the theory predicts the location of the above-mentioned nodal point fairly accurately. The effect of friction is significant in both profiles and hence the observed values of $u(y=0)$ are much smaller than the values predicted by the inviscid theory (which are $1/c$ times $\eta(y=0)$). We should also note that in figure 9(*c*) H_0 is smaller ($=0.05$ m) and the damping is stronger compared with figure 9(*b*) where H_0 is larger ($=0.2$ m). If the main features of the present channel theory are relevant to observations on continental shelves, these distinct features of the non-harmonic solution should be detectable in coastal studies.

The theory in this work is a result of a two-year research funded by the Israel Sciences Foundation under grant number 579/09 to H.U. The experimental part was funded by the 6th framework programme (Structuring the European Research Area) of the European Commission, within the Integrated Infrastructure Initiative Hydralab-III. The technical support provided by H. Didelle and S. Viboud at LEGI/Coriolis is highly appreciated. The comments of three anonymous reviewers have greatly improved the presentation of the ideas developed in this study.

REFERENCES

Abramowitz, M. & Stegun, I. A. 1972 *Handbook of Mathematical Functions*. Dover.

Buchwald, V. T. & Adams, J. K. 1968 The propagation of continental shelf waves. *Proc. R. Soc. Lond.* A**305**, 235–250.

Caldwell, D. R., Cutchin, D. L. & Longuet-Higgins, M. S. 1972 Some model experiments on continental shelf waves. *J. Marine Res.* **30**, 38–55.

Cartwright, D. E. 1969 Extraordinary tidal currents near St. Kilda. *Nature* **223**, 928–932.

Cushman-Roisin, B. 1994 *Introduction to Geophysical Fluid Dynamics*. Prentice-Hall.

Cutchin, D. L. & Smith, R. 1973 Continental shelf waves: low-frequency variations in sea level and currents over the Oregon continental shelf. *J. Phys. Oceanogr.* **3**, 73–82.

De-Leon, Y. & Paldor, N. 2009 Linear wave in mid-latitudes on the rotating spherical Earth. *J. Phys. Oceanogr.* **39**, 3204–3215.

Gill, A. E. 1982 *Ocean-Atmosphere Dynamics*. Academic Press.

Hamon, B. V. 1962 The spectrum of mean sea level at Sydney, Coff's Barbour and Lord Howe Island. *J. Geophys. Res.* **67**, 5147–5155.

Hamon, B. V. 1966 Continental shelf waves and the effect of atmospheric pressure and wind stress on the sea level. *J. Geophys. Res.* **71**, 2883–2893.

Ibbetson, A. & Phillips, N. 1967 Some laboratory experiments on Rossby waves in a rotating annulus. *Tellus* **19**, 81–87.

Mooers, C. N. K. & Smith, R. L. 1968 Continental shelf waves off Oregon. *J. Geophys. Res.* **73**, 549–557.

Mysak, L. A. & Hamon, B. V. 1969 Low frequency sea level behavior and continental shelf waves off North Carolina. *J. Geophys. Res.* **74**, 1397–1405.

Paldor, N., Rubin, S. & Mariano, A. J. 2007 A consistent theory for linear waves of the shallow-water equation on a rotating plane in midlatitudes. *J. Phys. Oceanogr.* **37**, 115–128.

Paldor, N. & Sigalov, A. 2008 Trapped waves on the mid-latitude β-plane. *Tellus* A **60** (4), 742–748.

Pedlosky, J. 1986 *Geophysical Fluid Dynamics*, 2nd ed. Springer.

Phillips, N. A. 1965 Elementary Rossby waves. *Tellus* **17**, 295–301.

Pierini, S., Fincham, A. M., Renouard, D., Rosaria, M. & Didelle, H. 2001 Laboratory modeling of topographic Rossby normal modes. *Dyn. Atmos. Oceans* **35**, 205–225.

Platzman, G. W. 1968 The Rossby wave. *Quar. J. Met. Soc.* **94**, 225–246.

Rhines, P. 1970 Edge-, bottom-, and Rossby waves in a rotating stratified fluid. *Geophys. Fluid. Dyn.* **1**, 273–302.

Staniforth, A. N., Williams, R. T. & Neta, B. 1993 Influence of linear depth variation on Poincare, Kelvin, and Rossby waves. *J. Atmos. Sci.* **50** (7), 929–940.

Sumathi, S. & Surekha, P. 2007 *LabVIEW Based Advanced Instrumentation Systems*. Springer.